X-ray pinhole camera resolution and emittance measurement

Cyrille Thomas,* Guenther Rehm, and Ian Martin
Diamond Light Source, Oxfordshire, OX11 0DE, United Kingdom

Riccardo Bartolini
Diamond Light Source, Oxfordshire, OX11 0DE, United Kingdom,
and John Adams Institute, University of Oxford, OX1 3RH, United Kingdom
(Received 30 January 2009; revised manuscript received 1 December 2009; published 24 February 2010)

Third generation synchrotron light sources are characterized by a low emittance and a low emittance coupling. Some light sources are already operating with extremely low coupling close to 0.1%. Measurement of the transverse beam size is generally used to measure the emittance and the coupling. To this end, several systems are currently used and an x-ray pinhole camera is one of them. In this paper we derive the point spread function of the x-ray pinhole camera both analytically and numerically using the Fresnel diffraction integral and taking into account the broadband spectrum of the bending magnet source, and we show that an optimized design allows the measurement of extremely small vertical beam sizes below 5 μm. The point spread function of several scintillator screens is also measured, and it shows that the contribution of the diffraction and the screen point spread functions have to be taken into account for an accurate measurement of a low coupling. Finally, we show measurements of the vertical beam sizes as small as 6 μm for our nonoptimized setup.

DOI: 10.1103/PhysRevSTAB.13.022805 PACS numbers: 07.85.Fv, 87.59.−e, 29.27.−a, 41.50.+h

I. INTRODUCTION

Third generation synchrotron light sources are characterized by low emittance, and with the top-up operation becoming routine, they can afford (in terms of reduced lifetime) to operate at extremely low emittance coupling [1]. The measurement of the emittance can be done indirectly by measuring the transverse beam size using the synchrotron radiation produced by it. To this end, several methods, namely visible light imaging, x-ray imaging using Fresnel zone plates, compound refractive lenses or a pinhole camera, and interferometric techniques, are currently used. All these systems have advantages but also limitations. Visible light imaging is limited in resolution by diffraction of synchrotron radiation. For the case of Diamond, the typical synchrotron radiation diffraction spot size at 400 nm is ≈ 50 μm. Fresnel zone plates using x rays present the best possible resolution [2] but they require monochromatic beam and the whole system can require significant effort to bring into routine operation [3]. In addition, the combination of a small zone width and a large thickness constitutes a major fabrication challenge, especially for hard-x-ray Fresnel zone plates.

Similarly, image formation can be achieved using compound refractive lenses [4] with x rays; however, these also require monochromatic light as they will introduce large chromatic aberrations, limiting the resolution of the system. Beam size measurement using interference methods also requires monochromatic light, and in the visible has a better resolution than imaging systems. However, due to the natural opening angle of the synchrotron radiation [5,6], the maximum distance between the two slits is limited. In the visible range and for medium energy machines, i.e., for maximum opening angle between the slits of the order of 5 mrad, this leads to a minimum measurable vertical beam size in the range of 20 μm. Another method for measuring the beam size consists of measuring the profile of the vertical π polarization of the bending magnet radiation [1]. This method has recently shown the capability to accurately measure vertical beam sizes as small as 6 μm. However, this method requires significant experimental effort as well as extensive computations to establish routine operation.

At Diamond, we have chosen to use two x-ray pinhole cameras imaging the electron beam from two bending magnets, as they offer the required resolution and the dynamic range to accurately measure the electron beam size, typically (50×25) μm^2 for 1% coupling, at all currents from below 1 to 500 mA [7]. Like any other optics system, it suffers from chromatic effects, and a nonoptimized system may prevent measurement of an extremely small beam size. However, optimization of the x-ray pinhole system will give the possibility to measure very small beam sizes of typically less than 5 μm.

In the following section we calculate the point spread function of the pinhole camera using analytical expressions. In Sec. III we present a general approach to calculate the point spread function (PSF) of the pinhole and introduce scaling parameters applied to the square aperture. In Sec. IV, we analyze the case of the square aperture for a large bandwidth source, and apply it to the case of Diamond. Finally and before concluding, we present ex-

*cyrille.thomas@diamond.ac.uk

perimental results for the calculation of the resolution of the pinhole camera at Diamond and the measurement of very small vertical beam size of the order of 6 μm.

II. POINT SPREAD FUNCTION OF THE X-RAY PINHOLE CAMERA: ANALYTICAL APPROACH

The image formed on the camera is the convolution of the source profile, and of the PSF of the diffraction through the pinhole, and of the PSF of the x-ray camera. Consequently, the convolved PSF of the diffraction and of the camera determines the smallest image size measurable by the imaging system. Let us call Σ the rms Gaussian size of the image of the electron beam and assume the source and the PSF to be Gaussian. In that particular case, Σ can be expressed as follows:

$$\Sigma^2 = S^2 + S^2_{\text{pinhole}} + S^2_{\text{camera}}, \tag{1}$$

where S is the rms size of the image of the photon beam located at the distance d from the pinhole, S_{pinhole} is the diffraction rms size from the pinhole, and S_{camera} is the rms spatial resolution of the x-ray camera. We note that the PSF of the camera can be decomposed further as the x-ray camera has an x-ray screen, a lens, and a CCD chip; however, we consider this system as a whole with its own PSF.

Equating S to zero in expression (1) gives the point spread function width of the system, Σ_0. Let us focus on the PSF width of the diffraction through the pinhole. This contribution can be decomposed in two parts: the diffraction from the pinhole, S_{diff}, and the geometrical contribution due to the finite size of the pinhole, S_{aperture}: $S^2_{\text{pinhole}} = S^2_{\text{diff}} + S^2_{\text{aperture}}$. Figure 1 shows the schematic for the pinhole camera system and the decomposition of the PSF.

The contribution of the diffraction to Σ_0 is given analytically by [8]

$$S_{\text{diff}} = \frac{\sqrt{12}}{4\pi}\frac{\lambda D}{A} \tag{2}$$

and

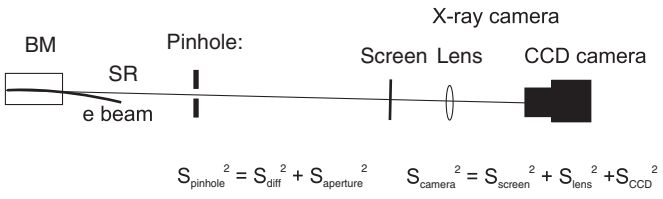

FIG. 1. Schematic of the pinhole camera system and the decomposition of the PSF. The relativistic electron beam (e beam) goes through a bending magnet (BM), emitting synchrotron radiation (SR). The electron beam is imaged by the pinhole onto the x-ray camera. For each element having a PSF Gaussian, the total PSF, $\Sigma^2_0 = S^2_{\text{pinhole}} + S^2_{\text{camera}}$.

$$S_{\text{aperture}} = \frac{A}{\sqrt{12}}\frac{(D+d)}{d}, \tag{3}$$

where d is the distance source pinhole and D pinhole image, λ is the wavelength, and A the pinhole aperture.

The optimum aperture that minimize the point spread function is

$$A_0^2 = \frac{12}{4\pi}\frac{\lambda d D}{d+D}. \tag{4}$$

Pinhole cameras at Diamond

In the case of Diamond, two pinholes and two x-ray imaging devices are placed at two different bending magnet locations. The first location, which we call pinhole 1, has its pinhole at 3.76 m from the source at 11.3 mrad from the straight. The image is 9.05 m behind the pinhole. The second location, which we call pinhole 2, has its pinhole at 4.45 m from the source at 23.7 mrad from the straight. The image is 11.92 m behind the pinhole. Both pinholes can be chosen from an array of nine pinholes combination of 25, 50, and 400 μm apertures, although the smallest aperture is always used for measurements. Assuming monochromatic light, Fig. 2 shows the optimum apertures as a function of photon energy for the case of these two pinholes.

However, the synchrotron radiation is passed from vacuum to air through a 1 mm thick aluminum window, which acts also as a filter. The pinholes and the x-ray camera are in air, which results in additional filtering of the x-ray spectrum through the air path. Therefore, the source has

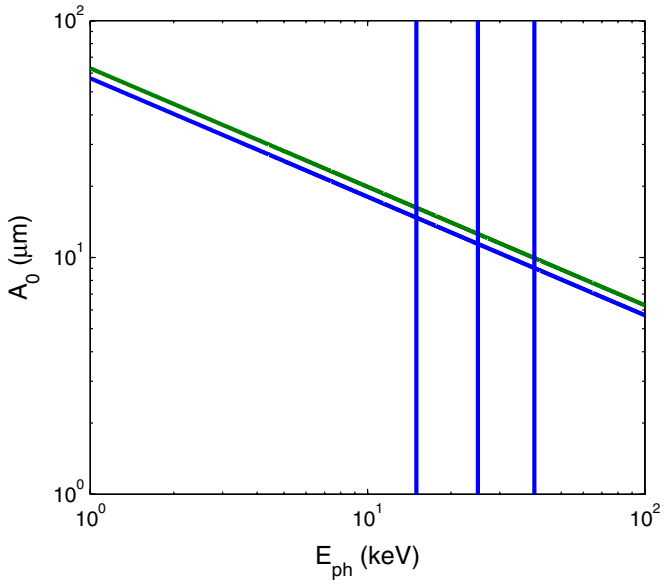

FIG. 2. (Color) Optimum pinhole aperture vs photon energy. The vertical lines show photon energies at 15, 25, and 40 keV, which are close to the minimum energy filtered by the Al window, close to the peak and some higher photon energy, respectively.

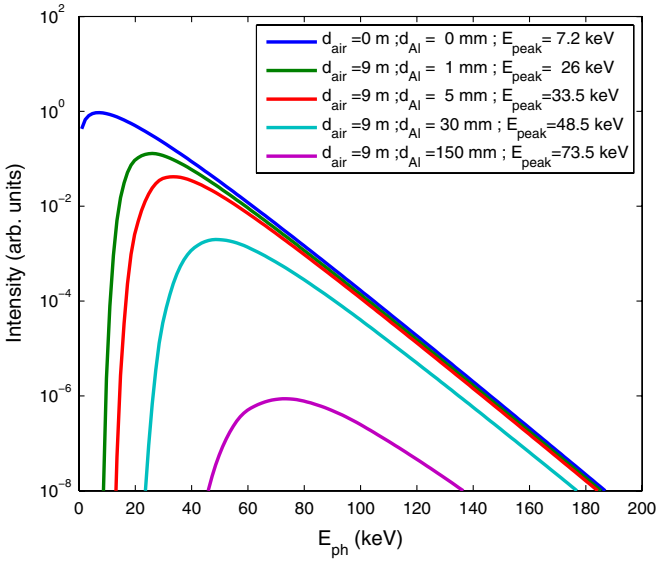

FIG. 3. (Color) Spectrum of the synchrotron radiation in vacuum and also filtered by Al window and 9 m of air (for the case of Diamond). The thickness of the Al window and the peak of the spectrum are shown in the legend. We have chosen an extreme case with an Al window of 150 mm in order to show a large shift towards the higher energies, which could be exploited in higher energy machines than Diamond as the flux also would be higher.

a spectrum from approximately 15 keV to above 60 keV, and peaks around 26 keV (see Fig. 3). The optimum aperture can be estimated with the analytical expression (4) at the peak of the power spectrum of the source. In our case, the peak for our two pinholes is around 26 keV. The optimum apertures are $A_0 \approx 11.0$ μm and $A_0 \approx 12.0$ μm for pinhole 1 and pinhole 2, respectively.

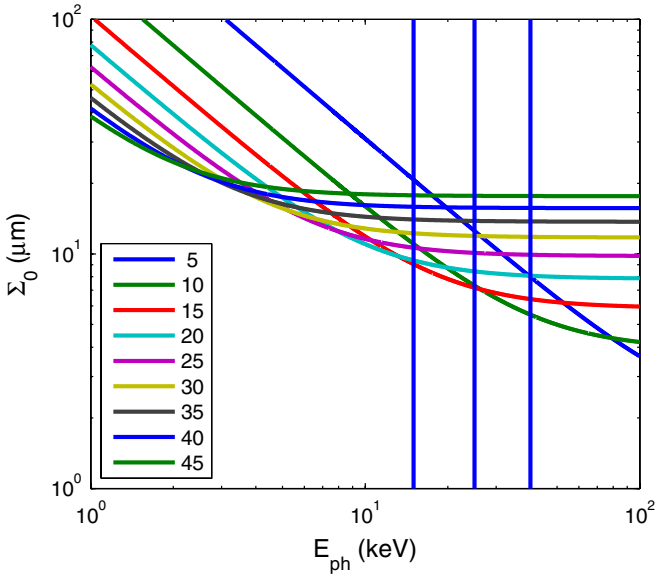

FIG. 4. (Color) PSF rms width vs photon energy for several apertures in pinhole 2.

Figure 4 shows the PSF rms width for pinhole 2 as a function of the photon energy without the contribution of the x-ray camera, i.e. $\Sigma_0 \equiv S_{\text{pinhole}}$. It can be noted that for high photon energy the width is dominated by S_{aperture}. For our 25 μm pinhole aperture, $S_{\text{pinhole}} \approx 10$ μm for both pinholes, whereas it would be $S_{\text{pinhole}} \approx 6$ μm at the optimum aperture of 11.0 and 12.0 μm for pinholes 1 and 2, respectively.

III. NUMERICAL APPROACH IN THE FRESNEL APPROXIMATION

The light source from the bending magnet has a broad spectrum from infrared to hard x ray. In our case, due to the Al window, the bandwidth of the source goes from approximately 15 keV to above 60 keV. A more accurate model of the PSF needs to take into account the broad spectrum of the bending magnet synchrotron radiation, and the fact that the screen is almost always in the near field range. Therefore, a more general approach to calculate the PSF from the pinhole is to compute the illumination on a screen through the pinhole from a source point using the Fresnel diffraction theory. To calculate the PSF using Fresnel diffraction theory we need to satisfy the following conditions: we consider a filament of electrons as our point source; the synchrotron radiation satisfies the scalar propagation equation; the distances on the screen and the aperture of the pinhole satisfy the paraxial approximation. In addition we assume the pinhole to be uniformly illuminated. Once these assumptions are satisfied, one can calculate the electric field on the screen using [9,10]

$$E_\lambda(x, y, z) = E_{0\lambda}(x, y, z)\alpha_F(x, y, z), \tag{5}$$

where

$$E_{0\lambda}(x, y, z) = E_0 \frac{e^{ik(r_0+r)}}{r_0 + r}$$

is the geometrical field at the point of observation P according to Huygens-Fresnel's principle, and $\alpha_F(x, y, z)$ is the modification of the geometrical field by diffraction through the aperture, $E_0(P)$ is the normally incident geometrical irradiance at P; r_0 represents the distance between the point source $P_0(x_0, y_0, z_0)$ and the intersection $M(x_M, y_M, 0)$ of the aperture plan and the line P_0P, and r the distance between M and P (see Fig. 5).

We can express α_F and then the intensity on a screen for the particular case where the aperture is a square pinhole, with the source illuminating the pinhole uniformly:

$$I_\lambda(x, y, z) = I_{0\lambda}(x, y, z) \left| \int_{-a}^{a} e^{i2\pi[(\xi - x_M)^2/2\lambda\rho]} d\xi \right. \times \left. \int_{-b}^{b} e^{i2\pi[(\eta - y_M)^2/2\lambda\rho]} d\eta \right|^2, \tag{6}$$

with (x_M, y_M) the intersection point between the aperture and the straight P_0P; λ is the wavelength of the emitted

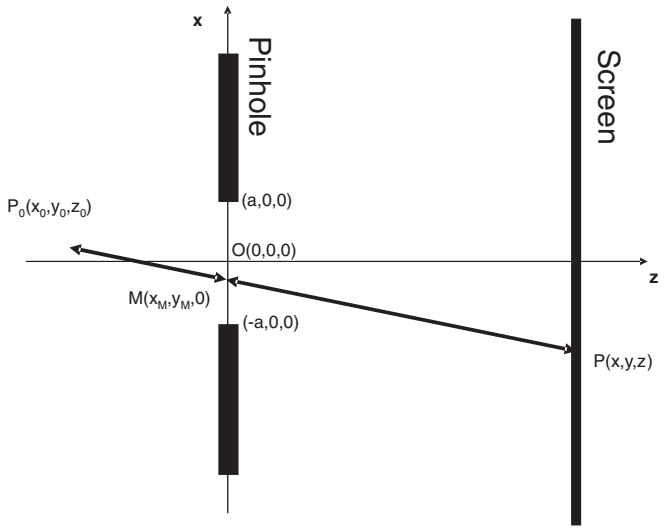

FIG. 5. Geometry of the square aperture for the calculation of the Fresnel integral.

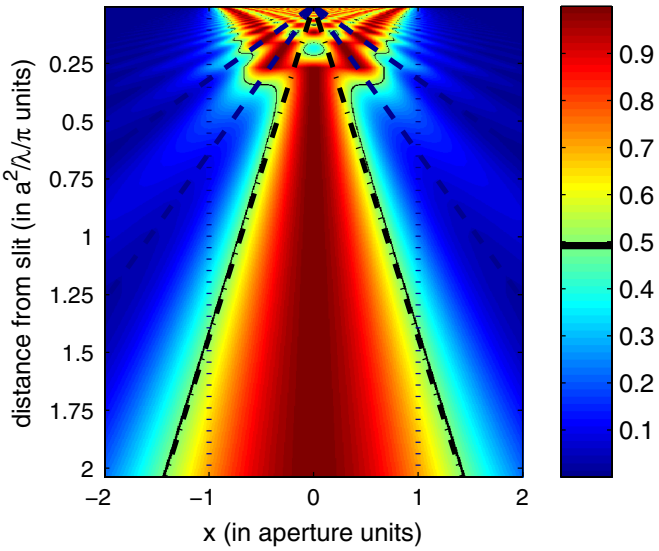

FIG. 6. (Color) Normalized Fresnel diffraction through a slit (maximum is equal to 1), varying the distance pinhole screen, z, and for source at infinity. The horizontal axis is expressed in units of the half-aperture a, and the vertical axis shows the variation of z as $Z = \frac{z\lambda}{a^2}$. The dashed lines represent the first and second zeros of the far-field solution. The black line is the FWHM of the near field solution, and the dash-dotted line its asymptotic behavior. The dotted lines represents the aperture.

light and $\rho = -[(zz_0)/(z - z_0)]$ $(z_0 < 0)$. The apertures of the pinhole are $2a$ and $2b$ in each axis.

For numerical convenience, it can be shown that expression (6) is also a Fourier transform of the function f with the change of variable $\lambda\rho\nu = \xi$ and $\lambda\rho\mu = \eta$:

$$\begin{aligned} &w = a, b; \qquad \kappa = \nu, \mu \qquad f(\kappa) = e^{i\pi\kappa^2\lambda\rho} \\ &\forall|\kappa| < \frac{w}{\lambda\rho} \qquad f(\kappa) = 0 \qquad \forall|\kappa| > \frac{w}{\lambda\rho}. \end{aligned} \tag{7}$$

Then expression (6) becomes

$$\begin{aligned} I_\lambda(x,y,z) = 4I_{0\lambda}(x,y,z)(\lambda\rho)^2 |e^{i2\pi(x_M^2/2\lambda\rho)}|^2 |e^{i2\pi(y_M^2/2\lambda\rho)}|^2 \\ \times \left| \int_{-\infty}^{\infty} e^{i\pi\lambda\rho\nu^2} e^{-i2\pi\nu x_M} d\nu \right|^2 \\ \times \left| \int_{-\infty}^{\infty} e^{i\pi\lambda\rho\mu^2} e^{-i2\pi\mu y_M} d\mu \right|^2, \end{aligned} \tag{8}$$

where the phase terms $|e^{i2\pi(x_M^2/2\lambda\rho)}|^2 = |e^{i2\pi(y_M^2/2\lambda\rho)}|^2 = 1$ and the integrals are the Fourier transform of the function f.

In the following we will mainly use expression (8) to calculate the PSF of the pinhole. In Sec. III A we apply expression (8) to the case of a slit, and we show some remarkable general results in normalized variables.

A. General case of slit diffraction in the Fresnel approximation

The diffraction from the square aperture is reduced to the slit aperture by calculating only one integral using expression (8) or (6). Furthermore, the results can be normalized. Figure 6 shows such a normalization: first, it is expressed in normalized units, $\frac{\rho\lambda}{a^2}$ and x/a for the vertical and horizontal axis, and second, we have normalized the maximum of the PSF to 1 for each value ρ. This last normalization masks the decay of intensity with distance. The figure represents the normalized Fresnel diffraction through a slit, calculated with expression (8), for a given wavelength λ and aperture $2a$, at almost infinite distances z_0 and varying only z, in which case $\rho \approx z$. As for any other aperture shape there is an optimum point where the width of the PSF is minimum and the peak intensity is maximum [10]. In the case of the square aperture and for the source at finite distance, the optimum point is given by $2\lambda\rho = \pi a^2$. For the source at infinity, this point is around $2\lambda z = \pi a^2$. In the figure, the black plain lines represent the FWHM of the PSF and in normalized units. At the optimum point the FWHM is $\Delta_{\mathrm{PSF}} \approx 0.7a$.

However, this is valid for monochromatic light only, and when the spectral bandwidth of the source is large, the chromatic effect needs to be taken into account. In such a case, the PSF may need to be calculated numerically. This will be done in the next section where we consider the more specific case of Diamond.

B. Image formation and deconvolution

The image formed on the camera is the result of a convolution with the PSF of the imaging system. In order to correctly measure the actual size of the object, it is important to deconvolve the image with the imaging system PSF, in particular when operating near its resolution limit. If the PSF is a Gaussian function, then deconvolution can easily be done with quadratic subtraction as given by the expression (1). In the general case, when the PSF is not

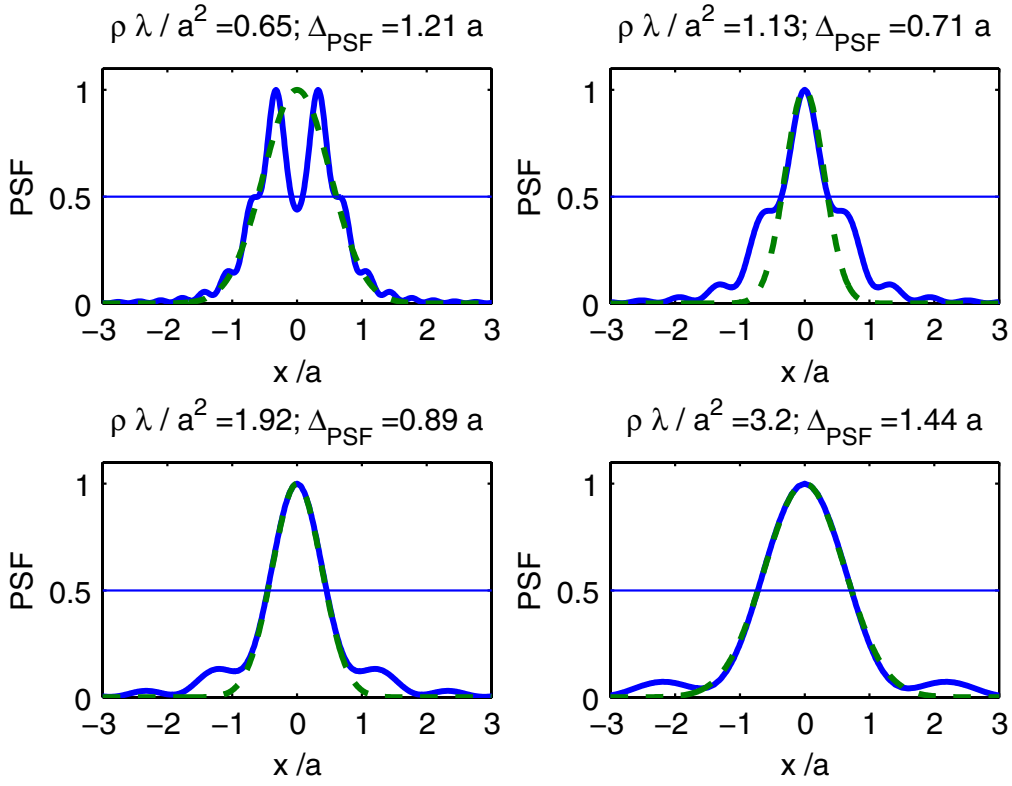

FIG. 7. (Color) Normalized PSF and comparison with a Gaussian of the same FWHM.

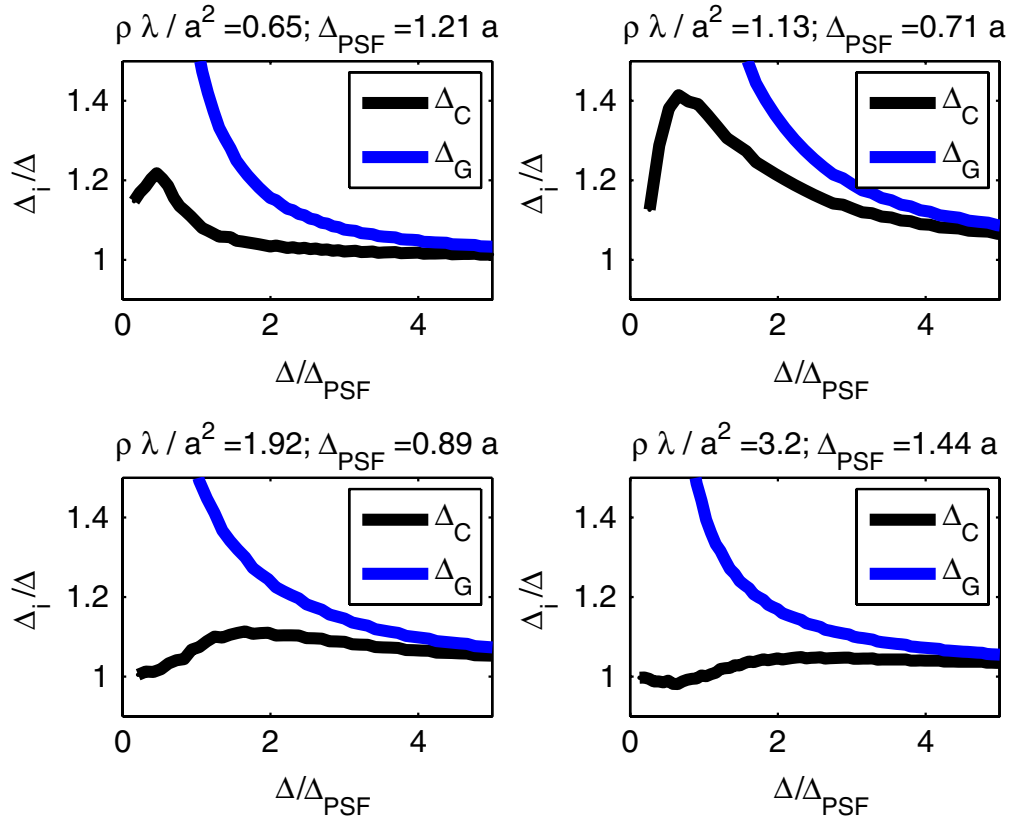

FIG. 8. (Color) Relative increase of the measured FWHM width introduced by convolution with the PSF and partial deconvolution with a Gaussian of the same FWHM width.

a Gaussian function, this quadratic sum can only be seen as an approximation. In this case, full deconvolution needs to be done, but this requires a precise knowledge of the PSF. Some examples of PSF for slits (one dimension of a square pinhole) are shown in Fig. 7 by extracting from Fig. 6 for several normalized distances.

It can be seen that the degree of quality to which these PSF can be approximated by a Gaussian varies. We found that a Gaussian of the same FWHM generally is closer than a Gaussian with the same rms as the PSF.

Next, the error produced by using the Gaussian approximation for deconvolution can be investigated. To this end, we simulate convolution of an image (a Gaussian distribution with FWHM Δ) with the PSF given by expression (8).

Figure 8 compares the relative size of the convolved image Δ_G to the corrected size $\Delta_C = \sqrt{\Delta_G^2 - \Delta_{\mathrm{PSF}}^2}$, where Δ_{PSF} is the FWHM of the PSF, as a function of the image size normalized to the PSF width. It can be seen that the correction applied by the quadratic subtraction is not perfect; a perfect correction would result in $\Delta_C/\Delta = 1$. The blue curves Δ_G/Δ represent the error without any correction. The real image size is always smaller than the size corrected by quadratic subtraction of the PSF size. We thus consider it prudent to use the PSF size for quadratic deconvolution down to measured beam sizes in the order of Δ_{PSF}.

IV. PSF OF THE SQUARE APERTURE FOR LARGE BANDWIDTH

Figures 9(a)–9(d) show the diffraction for a slit in the vertical plane and for apertures varying from 50 to 5 μm, for the case of Diamond. On the top of the image we have plotted the sum over the photon energies of the diffraction patterns, and on the right of the image the intensity distribution as a function of the photon energy, filtered by the 1 mm thick Al window (see also Fig. 3. For the 50 μm aperture, the characteristic flattop of the Fresnel diffraction can be seen. With decreasing aperture, the diffraction pattern becomes closer to the far-field diffraction pattern, which is described by the analytical function $|\sin(x)/x|^2$. Indeed, the smaller the aperture the smaller the Fresnel number ($N_F = 4a^2/\lambda z$) becomes; in other words, the wave front correction introduced in the integral is less varying across the aperture, and the plane-wave approximation

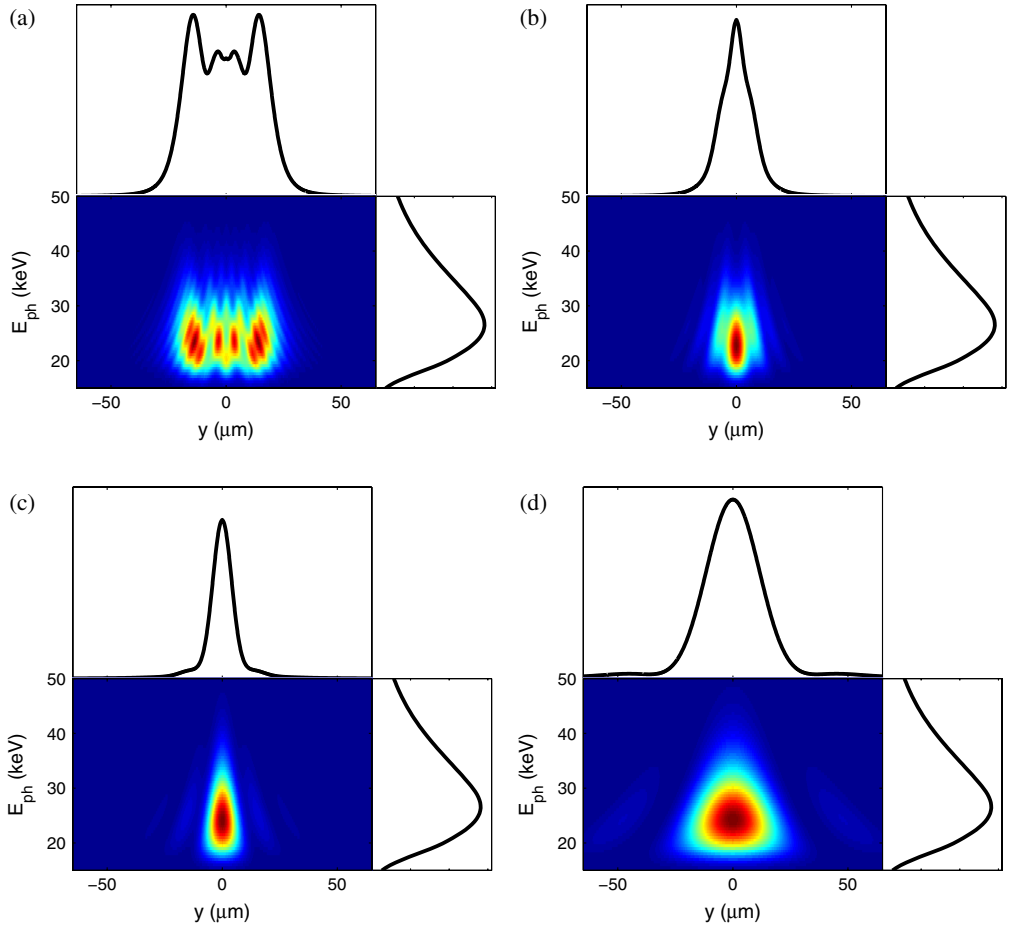

FIG. 9. (Color) Fresnel diffraction of the synchrotron radiation in pinhole 2 through several apertures: 50 μm (a), 25 μm (b), 15 μm (c), and 5 μm (d).

becomes more valid. Conversely, the larger the Fresnel number, the more pronounced the flattop distribution is, leading to an image dominated by the geometrical contribution from the aperture.

A. Fresnel diffraction: Large bandwidth source, varying aperture, and distance

The PSF depends on the spectrum, the aperture and the conjugate object, and image distances. In order to investigate this we calculate the PSF for the spectra shown in Fig. 3, varying the aperture and the distance pinhole screen; the distance pinhole source has been set to 3.8 m. We then extracted the width of each PSF and reported it in Fig. 10. All the curves present a similar behavior. As expected, for large aperture the PSF is aperture dominated and the width varies linearly with aperture. For small aperture, the PSF is closer to the far-field picture given by the $|\sin(x)/x|^2$ function. The width is inversely proportional to the aperture.

As can be observed in Fig. 10, the FWHM of the PSF as a function of magnification and aperture exhibits a minimum for each given source spectrum, which can be regarded as the optimum working point. In Fig. 11 we computed this optimum working point and reported the

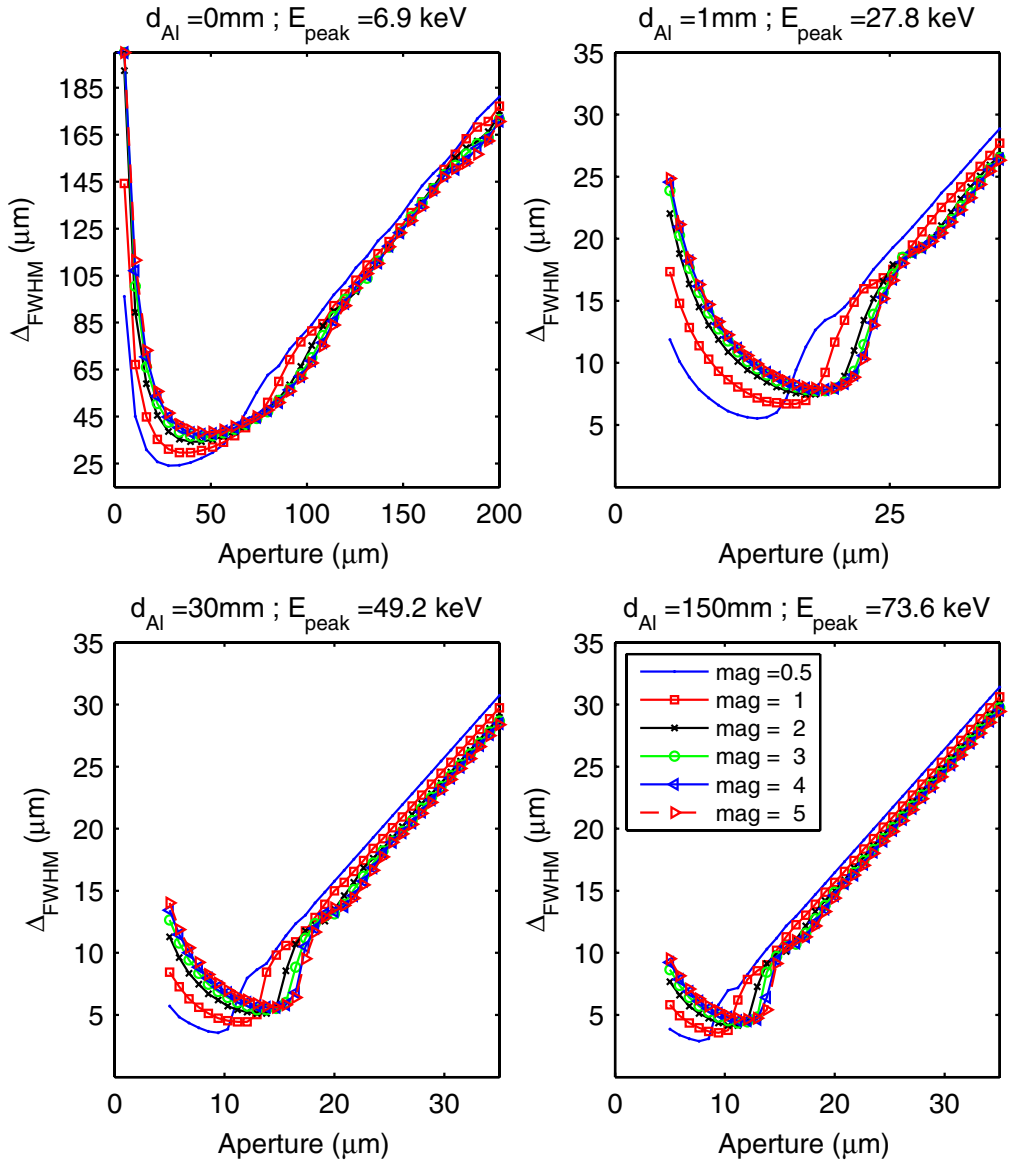

FIG. 10. (Color) Dependence of the PSF (FWHM) of the pinhole as a function of the aperture, and for several magnifications and several spectra (related to the filtering from air and Al thickness). The peak of the spectrum is indicated. In the first case, with no Al filter, we consider the case of a pinhole in vacuum. The distance source pinhole is 3.8 m and the distance pinhole screen varies. After the Al window, at the pinhole, the beam is further filtered by air.

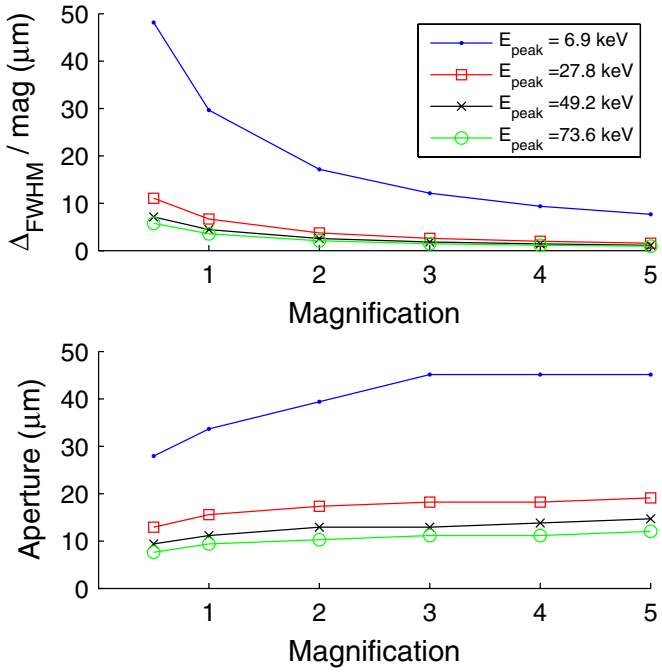

FIG. 11. (Color) Apparent point source size at the optimum aperture as a function of the magnification for the four cases shown in Fig. 10.

corresponding width divided by the magnification together with the corresponding optimum apertures, as a function of the magnification. The upper graph shows the minimum observable beam size (FWHM) at the optimum pinhole apertures (lower graph). The optimum width of the PSF does not increase linearly with the magnification, hence providing also a possibility to further optimize the pinhole camera resolution with a high magnification. However, this further optimization might be limited by the photon density decreasing with increasing magnification. A magnification between 2 and 3 appears to be a good compromise between resolution and photon density on the camera.

B. Application to the pinhole optimization at diamond

The PSF given by the Fresnel integral is not Gaussian. However, as stated above, we will use the full width half maximum of the integrated diffraction pattern, and we divided it by 2.35 in order to compare it with the analytical analysis, which assumes a Gaussian distribution. We have calculated the PSF as a function of the pinhole aperture, the spectrum, and at the distances for the two pinholes. Figure 12 shows the corresponding FWHM of the PSF for the case of pinhole 2. In the experimental setup, the Al thickness traversed by the photons can be varied from 1 to 12 mm by means of an Al wedge, thus varying the spectra as shown in Fig. 3.

Table I summarizes the width of the PSF found for the actual pinhole size at Diamond (25 μm) and the optimum apertures, for several Al attenuation lengths. It can be

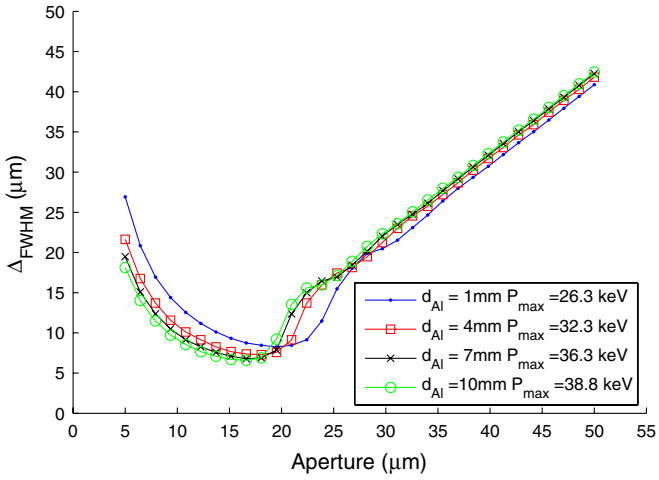

FIG. 12. (Color) FWHM of the PSF of pinhole 2 as a function of the slit apertures and for several thickness of Al filter.

noted that the width at the optimum aperture is always larger compared to the optimum found for the monochromatic case, i.e. $\Sigma_{PSF} \approx 0.7a/2.35$, where a is the half aperture. In addition, looking at the data for pinhole 1, it can be noted that a 45% increase in peak photon energy brings only a 28% decrease in resolution. Shifting the spectrum towards the higher energies does decrease the PSF width but not in a linear way and certainly at the cost of the photon flux. Finally, the PSF width given by the analytical expressions (2) and (3) gives the same general behavior as the numerical results. However, the optimum width is 2 times larger for an aperture almost 50% smaller than given by the numerical results.

TABLE I. FWHM/2.35 of the PSF of the x-ray pinhole Δ_{PSF}, given by the Fresnel expression (8), for the nominal (nom.) and optimum (opt.) slit apertures w, and for several Al filter lengths d_{Al}, at pinhole 1 and pinhole 2; and comparison with the analytical expression (rms) given by (2) and (3).

d_{Al} (mm)	1		4		7		10	
P1: E_{peak} (keV)	25.8		31.8		35.8		38.3	
P2: E_{peak} (keV)	26.3		32.3		36.3		38.8	
Numerical results (all in μm)								
	w	Δ_{PSF}	w	Δ_{PSF}	w	Δ_{PSF}	w	Δ_{PSF}
P_1 (nom.)	25	7.1	25	7.1	25	7.3	25	7.5
P_1 (opt.)	18.2	3.2	16.9	2.8	15.6	2.6	14.3	2.5
P_2 (nom.)	25	6.9	25	7.3	25	7.1	25	7.1
P_2 (opt.)	19.5	3.5	18.2	3.0	16.9	2.9	16.8	2.8
Analytical results (all in μm)								
P_1 (nom.)	25	10.3	25	10.2	25	10.2	25	10.2
P_1 (opt.)	11.2	6.4	10.1	5.8	9.5	5.4	9.1	5.3
P_2 (nom.)	25	10.0	25	10.0	25	9.9	25	9.9
P_2 (opt.)	12.3	6.8	11.1	6.1	10.4	5.7	10.1	5.6

V. EXPERIMENTAL RESULTS

It is rather difficult to experimentally verify the pinhole camera PSF with our setup. The electron beam cannot be made infinitely small, and if it is very small, we have no other means to independently measure the beam size so that we could assess the contribution of the PSF to the measured beam size. Nevertheless, our attempt to estimate the PSF is done in two steps. First, we measure the PSF of the camera, and then we make use of our two pinholes to verify that the measured size corrected by the estimated PSF width for each pinhole satisfies the unique vertical emittance.

A. PSF of the x-ray camera

The x-ray camera is composed of an x-ray screen that converts absorbed x-ray photons into visible photons and a CCD camera that observes the screen through a macrolens with a magnification close to 1. In order to directly measure the PSF of the screen and camera system, we remove the pinhole and use the x-ray fan on the screen to illuminate an opaque mask with a sharp edge made by a tungsten bar covering part of the screen. We measured the system resolution for several screen materials in different thicknesses: P43 thickness 5 μm, $CdWO_4$ thicknesses 500 and 200 μm, and Lu:AG 400, 200, and 100 μm. Table II summarizes the results. The analysis performed is a fit using the error function as the step response of the screen to the sharp edge. The result of the fit gives the rms PSF of the x-ray imaging system. Figure 13 shows one such measurement with the P43 screen.

B. Vertical beam size measurement

We present here measurements of the electron beam size at the end of 2007. The pinhole cameras were equipped with a $CdWO_4$ screen, i.e., the rms resolution of the system is 15.3 and 15.1 μm for pinhole 1 and pinhole 2, respectively. Figure 14 shows an image of the electron beam taken from pinhole 1. Correction to the lattice has been performed, resulting in low coupling emittance and small beam size. The measured vertical image beam size is 20.9 μm. After quadratic subtraction using the estimated rms PSF width of 15.3 μm for pinhole 1, and dividing by the 2.4 magnification, the measured electron beam size is 5.9 μm.

TABLE II. Width of the PSF (rms) of the x-ray camera with several screens of different thicknesses (all dimensions are in μm). The error is given by the standard deviation of the fitted width per line on the digital image.

Thickness	P43	$CdWO_4$	Lu:AG
5	6.2 ± 0.39	···	···
100	···	7.45 ± 0.45	···
200	···	8.45 ± 0.45	8.70 ± 0.45
400	···	···	10.0 ± 0.45
500	···	13.5 ± 0.45	···

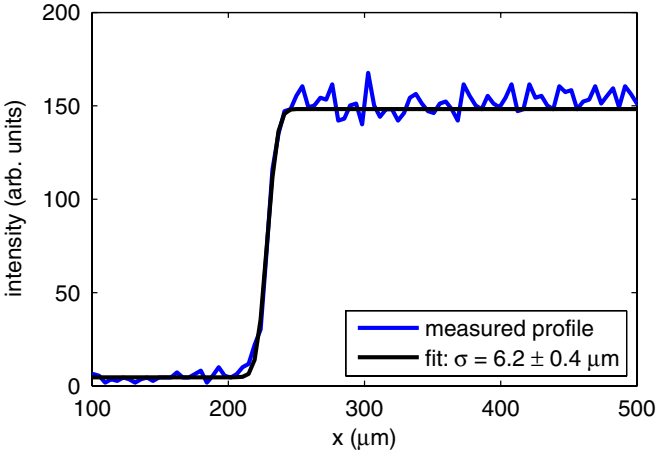

FIG. 13. (Color) Resolution of the x-ray camera with P43 screen, measured using the sharp edge from a tungsten bar in front of the screen. The rms resolution is $\Sigma_{\text{camera}} \approx 6$ μm.

We also measured the beam size against the lifetime as shown in Fig. 15. The camera setup is the same as above. The measurement has been done in a short time so that the conditions are the same across a set of skew quadrupole values. The horizontal beam sizes in pinhole 1 and pinhole 2 were constant at nominal values, 50 and 48 μm for pinhole 1 and pinhole 2, respectively. The curves are linearized with the quadratic correction, showing that the estimated resolution of the two systems is in agreement with the measurement. At a constant current, the linear behavior of the beam size vs lifetime is expected from a Touscheck lifetime limited beam. The slopes of the two corrected curves are 1.17 and 1.27 (μm/hour), agreeing with each other within 8%.

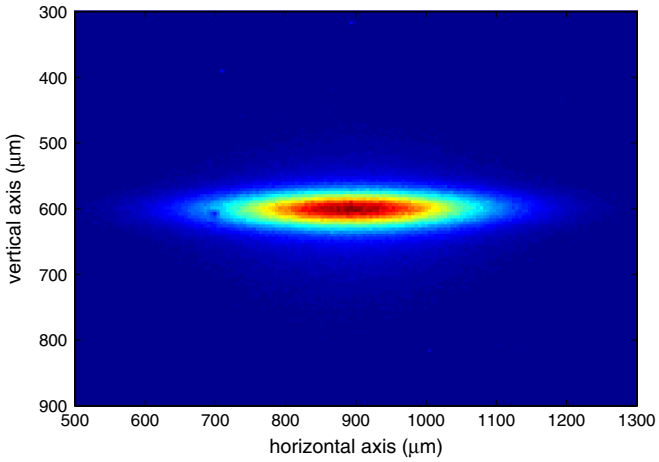

FIG. 14. (Color) Image from pinhole 1 with corrected optics for the storage ring, resulting in a low coupling and small beam size. The image beam size is 125.9 μm horizontally and 20.9 μm vertically.

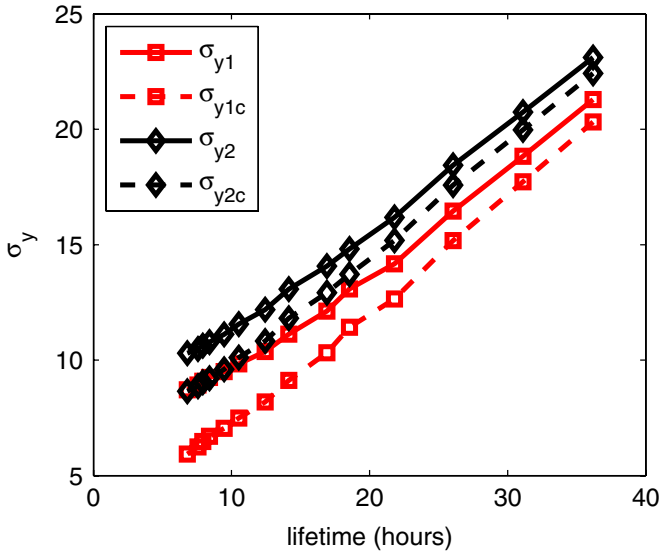

FIG. 15. (Color) Vertical beam size vs lifetime measured at the two pinholes.

In addition, the rms beam size, after quadratic subtraction of the estimated resolutions for the two pinholes, is 5.9 and 8.5 μm at the smallest coupling and for pinhole 1 and pinhole 2, respectively.

C. Emittance and emittance coupling

The horizontal emittance and the vertical emittance are calculated using the following formula:

$$\sigma_i^2 = \beta_i \epsilon_i + (\eta_i \sigma_\epsilon)^2, \tag{9}$$

where σ_i is the measured beam size in the horizontal or vertical plane, respectively ($i = x, y$), β_i and η_i are the betatron and dispersion functions at the source point and in the corresponding plane; and ϵ_i and σ_ϵ are the emittance and the relative energy spread of the electron beam. The vertical emittance is also measured in percentage, K, of the (horizontal) emittance.

In the horizontal plane, we measure the emittance and the energy spread, being the solution of the two coupled equations with two unknown given by expression (9) for each of the two pinholes. The parameters β_x and η_x are assumed to be known. In practice, we measure the dispersion by varying the storage ring rf frequency by 100 Hz and retrieving the slope of the linear displacement of the centroid of the electron beam measured by the pinhole images. We also check the agreement with the data given by the linear optics measurements and optimization procedure known as LOCO [11,12]. In general, the agreement with the dispersion value is better than 1%. For the measurement of the betatron function at the pinhole sources, we rely on the LOCO data and perform a quadratic fit to retrieve the value of the betatron function at the source points. In the calculation of emittance and energy spread, this value is a source of uncertainty. To minimize the uncertainty we include the pinhole positions in the LOCO measurement and verify the accuracy of the quadratic fit. The beam image horizontal rms sizes measured at the two pinholes are of the order of 120 μm. We have seen that the total PSF (rms), including the screen, is of the order of 15 μm or less. In this case, the error on the size measurement, $\Sigma_0^2/2S^2$, is less than 1%.

TABLE III. Vertical emittance measurements. Horizontal emittance and relative energy spread are measured close to the nominal values, i.e., 2.7 nm rad and 0.001, respectively. The betatron values are $\beta_{y,1} = 21.54$ m and $\beta_{y,2} = 23.38$ m. The magnification is $m_{1,2} = 2.4, 2.7$ for pinhole 1 and pinhole 2, respectively. η_i and Σ_i are measured values, and P stands for pinhole.

Date	η_y (mm)	Σ_y (μm)	σ_y (μm)	ϵ_y (pm rad)
			$= \sqrt{\Sigma_y^2 - \Sigma_0^2}/m_i = (\sigma_y^2 - \eta_y^2\sigma_\epsilon^2)/\beta_y$	
$CdWO_4$ screen: pinhole 1, 2 $\Sigma_0 = 15.3, 15.1$ (μm)				
10/07P 1	0.1	28	9.7	4.6
P 2	0.1	32	10.6	4.9
12/07P 1	0.7	21.5	6.3	1.8
P 2	0.25	23.4	6.7	1.6
P43 screen pinhole 1, 2 $\Sigma_0 = 9.6, 9.4$ (μm)				
01/08P 1	3	21	7.7	2.37
P 2	5	25	8.6	2.08
02/08P 1	0.1	19	6.8	2.18
P 2	0.9	21	6.9	2.10

In the vertical plane we assume the energy spread known, so we have two equations and only one unknown, i.e., the vertical emittance. After applying the correction from LOCO, the dispersion measured is generally less than 1 mm. For very small vertical emittance, the dispersion may contribute for 10% to 20% of the beam size measured so, even if it is small and could sometimes be neglected in the vertical emittance measurement, it is always taken into account. By applying corrections to the beam optics, we measured vertical beam sizes as small as 6 μm on both pinholes, which corresponds to a vertical emittance of $\epsilon_y \approx 1.7$ pm rad. From the analysis performed in Sec. III the quadratic correction overestimates the beam size measurement by up to 40%. However, this factor is difficult to measure experimentally, so the beam size measured is taken as an upper limit. Table III shows some of the results obtained with corrected optics. The good agreement between the two measurements is only due to the quadratic correction from the total PSF width.

VI. DISCUSSION AND CONCLUDING REMARKS

We have evaluated the PSF of the x-ray pinhole camera with a bending magnet source by computing the Fresnel diffraction PSF of a square aperture and measuring the PSF of the x-ray camera with a set of screens. With this we have

been able to accurately estimate the total PSF for the particular case of Diamond x-ray pinhole cameras, but also we have derived a method to optimize the parameters of the system for the best possible resolution. These parameters are the conjugated distances source pinhole and pinhole screen, the pinhole aperture, the spectrum of the source. It has also been shown that these parameters are not entirely free, i.e., for given distances and photon energy distribution, there is one aperture that minimizes the width of the PSF. The procedure to optimize the system should start with the given spectrum, and use it to find the best PSF as a function of distances and aperture. In the example treated, which is the case of pinhole 1 at Diamond, and for the case with 1 mm thick Al filter, the best PSF is 3.2 μm (rms), limiting the spectrum from 15 keV and above, a magnification 2.4, distance source pinhole 3.8 m and distance pinhole screen 9.0 m, and an aperture of 18 μm. This will give us the possibility to improve the resolution of our system, taking into account that our actual distances are fixed as the systems are installed in the storage ring tunnel, thus the distance source pinhole is already the smallest possible and the distance pinhole screen the longest possible. This leaves the aperture as an optimization parameter for the given spectrum.

Another remark can be made on the results obtained with the numerical evaluation of the PSF in comparison to the analytical expression which is often given as a reference. For the example of pinhole 1 and Al filter 1 mm thick in the optimized case, it is found that the source resolution is 1.33 μm (PSF FWHM/2.35 divided by the magnification, 2.4 is this case) at an aperture of 18.2 μm, which is twice better than the analytical estimation and for an aperture that is 50% larger.

The measurements of the PSF of a set of screens shows that its contribution to the total PSF is important but not entirely dominating as we had thought from previous publications. In fact, a very thin scintillator screen like $CdWO_4$ should reduce the PSF rms width further. However, this would be to the detriment of the flux of photons reaching the camera. In the optimum case described above, and a P43 screen with $\Sigma_{\mathrm{camera}} = 6.2$ μm, the rms width of the total PSF should be then $\Sigma_0 = 6.9$ μm. In such a case, our system would allow one to measure electron beam size as small as $6.9/2.4 = 2.9$ μm. This corresponds to a vertical emittance $\epsilon_y = 0.4$ pm, benefiting from the lattice parameters of modern machines that have in general a large vertical betatron value in the bending magnets, e.g., in this particular example $\beta_y = 21.5$ m.

[1] Å. Andersson, M. Böge, A. Lüdeke, V. Schlott, and A. Streun, Nucl. Instrum. Methods Phys. Res., Sect. A **591**, 437 (2008).

[2] Y. S. Chu, J. M. Yi, F. de Carlo, Q. Shen, W.-K. Lee, H. J. Wu, C. L. Wang, J. Y. Wang, C. J. Liu, C. H. Wang, S. R. Wu, C. C. Chien, Y. Hwu, A. Tkachuk, W. Yun, M. Feser, K. S. Liang, C. S. Yang, J. H. Je, and G. Margaritondo, Appl. Phys. Lett. **92**, 103119 (2008).

[3] H. Sakai, M. Fujisawa, K. Iida, I. Ito, H. Kudo, N. Nakamura, K. Shinoe, T. Tanaka, H. Hayano, M. Kuriki, and T. Muto, Phys. Rev. ST Accel. Beams **10**, 042801 (2007).

[4] A. Snigirev, V. Kohn, I. Snigireva, and B. Lengeler, Nature (London) **384**, 49 (1996).

[5] T. Mitsuhashi, Spatial Coherency of the Synchrotron Radiation at the Visible Light Region and its Application for Vertical Beam Profile Measurement, APS Meeting Abstracts, page 3 (1997).

[6] M. Arinaga, J. Flanagan, S. Hiramatsu, T. Ieiri, H. Ikeda, H. Ishii, E. Kikutani, T. Mimashi, T. Mitsuhashi, H. Mizuno, K. Mori, M. Tejima, and M. Tobiyama, Nucl. Instrum. Methods Phys. Res., Sect. A **499**, 100 (2003).

[7] C. A. Thomas and G. Rehm, in Proceedings of the Eleventh Beam Instrumentation Workshop 2004, Oak Ridge, TN, AIP Conf. Proc. No. 732 (AIP, Knoxville, Tennessee, 2004), pp. 182–189.

[8] P. Elleaume, C. Fortgang, C. Penel, and E. Tarazona, J. Synchrotron Radiat. **2**, 209 (1995).

[9] K. K. Sharma, *Optics: Principles and Applications* (Academic Press, New York, 2006).

[10] E. Hecht, *Optics* (Pearson Education, San Francisco, 2004), 4th ed.

[11] J. Safranek, Nucl. Instrum. Methods Phys. Res., Sect. A **388**, 27 (1997).

[12] J. Safranek, G. Portmann, A. Terebilo, and C. Steier, in *Proceedings of the 8th European Particle Accelerator Conference, Paris, 2002* (EPS-IGA and CERN, Geneva, 2002), pp. 404–406.